LASER & PHOTONICS REVIEWS
www.lpr-journal.org

Open-Path Dual-Comb Spectroscopy for Multispecies Trace Gas Detection in the 4.5–5 μm Spectral Region

*Fabrizio R. Giorgetta, Jeff Peischl, Daniel I. Herman, Gabriel Ycas, Ian Coddington, Nathan R. Newbury, and Kevin C. Cossel**

Open-path dual-comb spectroscopy provides multispecies atmospheric gas concentration measurements with high precision. Here, open-path dual-comb spectroscopy is extended to the mid-infrared 5 μm atmospheric window, enabling atmospheric concentration retrievals of the primary greenhouse gases, N_2O, CO_2, and H_2O, as well as the criteria air pollutants O_3 and CO across 600 m and 2 km round-trip paths. Measurements are demonstrated over a five-day period at 2 min temporal resolution with 80% uptime. The achieved precision is sufficient to resolve the atmospheric concentration variations of the multiple gas species; retrieved dry mixing ratios of CO and N_2O are in good agreement with a colocated point sensor. In addition, the retrieved ratio of excess CO versus CO_2 agrees with similar urban studies but disagrees with the US National Emission Inventory by a factor of 3. The retrieved ratio of excess N_2O versus CO_2 exhibits a plume-dependent value, indicating the variability of sources of the greenhouse gas N_2O.

1. Introduction

The 4.5–5 μm spectral region offers access to strong rovibrational spectral features of a number of important atmospheric trace gases including the greenhouse gases N_2O and CO_2 and the criteria air pollutants O_3 and CO. While CO_2 can also be detected with a simpler near-infrared (IR) dual-comb spectroscopy (DCS) system over open air paths, the three trace gases N_2O, O_3, and CO have much too weak a cross-section in the near-IR for detection at ambient levels; operation in this 4.5–5 μm spectral region enables their detection. In addition, this spectral region is relatively clear of strong water absorption features, which allows for open-path measurements over long distances.

Existing sensing technologies in this spectral region typically only measure one or two species; however, multispecies detection can be very beneficial for attributing sources. Open-path Fourier-transform infrared spectroscopy (OP-FTIR) can measure multiple gas species,[1] but the low spectral resolution (typically $\gtrsim$6 GHz) leads to potential issues with biases,[2,3] and very long open paths are challenging due to the incoherent light source's divergence. DCS[4] is an attractive platform for open-path measurements of multiple atmospheric species[5] that can overcome these limitations. Like FTIR, the broad spectral coverage of DCS allows for simultaneous quantification of many trace gas species as well as the path-averaged temperature. However, DCS has higher spectral resolution and negligible instrument line shape compared to OP-FTIR instruments, enabling trace gas concentration measurements at higher precision.[6] In addition, the comb lasers emit a bright, single transversal mode beam which can be propagated long distances, day or night, enabling continuous observation of gas concentrations and fluxes with high precision and over large areas.[7] These hectometer to kilometer scale open-path lengths reduce the sensitivity of the measurements to wind field errors and thereby reduce errors when quantifying emission rates of upwind sources. Finally, these path lengths are closely matched to the grid size of high-resolution (i.e., meso- and microscale) numerical weather prediction and air quality models, which reduces the model–measurement representation error.[8]

In previous work, an open-path DCS system in the near-infrared at 1.6 μm was used to simultaneously measure CH_4, CO_2, H_2O, and air temperature,[5,6] and the unique strengths of open-path DCS have enabled new measurement approaches for quantification of city scale CO_2 emissions,[7] detection of leaks in oil and gas infrastructure,[9,10] emissions from cattle feed lots,[11] and vertical/horizontal trace-gas profiling.[12] Here, our interest is to move into the 4.5–5 μm atmospheric window, which

Dr. F. R. Giorgetta, D. I. Herman, Dr. G. Ycas
Associate of the National Institute of Standards and Technology
National Institute of Standards and Technology
325 Broadway, Boulder, CO 80305, USA
Dr. F. R. Giorgetta, D. I. Herman, Dr. G. Ycas
Department of Physics
University of Colorado
Boulder, CO 80309, USA
J. Peischl
Cooperative Institute for Research in Environmental Sciences
University of Colorado
Boulder, CO 80309, USA
J. Peischl
Chemical Sciences Laboratory
National Oceanic and Atmospheric Administration
Boulder, CO 80305, USA
Dr. I. Coddington, Dr. N. R. Newbury, Dr. K. C. Cossel
Applied Physics Division
National Institute of Standards and Technology
325 Broadway, Boulder, CO 80305, USA
E-mail: kevin.cossel@nist.gov

The ORCID identification number(s) for the author(s) of this article can be found under https://doi.org/10.1002/lpor.202000583

DOI: 10.1002/lpor.202000583

can greatly expand the multispecies measurement capabilities of DCS and allows detection of critical atmospheric traces gases that are undetectable at ambient concentrations in the near-IR. Previous lab-based DCS systems that can potentially access this spectral band have been based on optical parametric oscillators,[13–16] interband and quantum cascade lasers,[17,18] and difference frequency generation (DFG) using supercontinua;[19–23] however, only a few DCS measurements have been demonstrated over atmospheric open air paths targeting ambient trace gases in the mid-infrared and all have been around 3 μm.[16,20,21,24] Here, we show a DFG-based dual-comb spectrometer capable of covering the 4.5–5 μm spectral region with comb-tooth resolution that can operate over long open air paths for the detection of multiple critical atmospheric trace gases at high sensitivity. We demonstrate simultaneous measurements of H_2O, N_2O, CO_2, CO, and O_3 across 600 m and 2 km long paths (one-way distances of 300 m and 1 km). We further show that the mid-infrared DCS instrument – despite the added complexity relative to near-infrared DCS – can provide high accuracy concentrations by comparing the retrieved N_2O and CO concentrations to an in situ point sensor. By measuring three critical atmospheric species not accessible to near-infrared DCS systems – CO, O_3, and N_2O – this spectrometer will enable future applications in understanding and monitoring urban air quality and greenhouse gas (GHG) emissions.

CO is important for air quality because it is a toxic gas and because it contributes to catalytic ozone production and destruction.[25] Globally, it also is the primary sink for the OH radical, which is the primary oxidant in the atmosphere and impacts the concentrations and distribution of greenhouse gases and pollutants. In addition, since CO is produced by incomplete combustion, it serves as a good tracer of anthropogenic emissions. For example, the ratio of CO to CO_2 can be used to track CO_2 emissions from fossil-fuel combustion and to distinguish different sources of combustion based on the combustion efficiency (e.g., power plants have a low ratio of CO to CO_2 compared to much less efficient nonroad vehicles).[26–28] In urban areas, the ratio of CO/CO_2 has been used to track diurnal variations in CO_2 source contributions[26] and to perform some CO_2 source sector attribution.[27] Furthermore, measurements of both CO and CO_2 in fire plumes can determine the modified combustion efficiency, which is a measure of the total carbon consumed and is important for better understanding the trace gas emissions from the fire.[29,30] Finally, because of the relatively long tropospheric lifetime (days to weeks),[25] CO also provides a tracer of long-range atmospheric transport, for example, from wildfires and urban areas.[28,31] Thus, open-path monitoring of CO, combined with numerical weather models, could be used to help identify the influence of wildfires, anthropogenic sources, and biogenic sources on urban air quality.

Ground-level O_3 is a major health hazard[32] and also has adverse impacts on vegetation and agriculture. In many regions, ground-level O_3 concentrations frequently exceed government control levels, thus there is a major emphasis on controlling and reducing O_3 levels. Tropospheric O_3 primarily arises from complex photochemical reactions of precursor species such as nitrogen oxides (NO and NO_2) as well as volatile organic compounds. The complex chemistry leads to significant challenges in developing a full understanding of ozone formation, especially in urban areas. Because of this complexity, state-of-the-art models still show persistent biases and often struggle to replicate high-O_3 events.[33] This can result in errors in exposure assessments and also complicates efforts to mitigate O_3. In many areas, wildfires and biomass burning are a potentially significant O_3 source; however, there is still uncertainty about the overall O_3 contribution from fires.[31] Simultaneous measurements of O_3 and CO could help to decrease this uncertainty. Furthermore, O_3 concentrations can have spatial gradients on the kilometer[34,35] and even tens-of-meter scale.[36] These gradients can lead to discrepancies between point measurements and models and their impact could be minimized with the long paths possible with DCS.

N_2O is the third most prevalent anthropogenic GHG. Measurement of N_2O is particularly challenging because the typical enhancements relative to atmospheric background levels are small (≈1% or less). Thus, compared to CO_2 and CH_4, the sources of N_2O are significantly less well-known as are the magnitudes of the feedback cycles influencing the sources.[37] The primary natural and anthropogenic sources arise from microbial activity in soils and can be driven by crop overfertilization.[37,38] Quantifying these emissions is challenging due to their large temporal and spatial variability,[39] but reliable monitoring of these emissions could improve agricultural efficiency while reducing environmental impact.[38] In urban areas, N_2O is primarily emitted from vehicles; however, N_2O is not routinely monitored in urban areas, so there are very few checks of emission inventories. As with CO, the ratio of N_2O to other gases can assist with source attribution. Improved determination of sector-specific emission ratios would allow high-resolution CO_2 emission inventories to be extended to other GHGs and criteria pollutants.[40]

Below, we first describe the 4.5–5 μm open-path DCS system, which probed both a 2 km and 600 m round-trip open path. In particular, we operated the system over the 600 m path for five days to compare the results with several in situ point sensors. We present precision analysis (Allan deviation) for the four species, N_2O, CO_2, CO, and O_3, and discuss potential systematic bias. Finally, we present example results analyzing the correlations of CO and N_2O with CO_2 for several plumes detected during the five days of measurement. While the system here is configured to target CO and N_2O, the optical backbone of the system follows that of a near-infrared DCS, which can precisely measure CO_2 and CH_4. Therefore, with some additional optical reconfiguration, a dual-channel near-/mid-IR could potentially monitor all urban GHG emissions.

2. Experimental Setup

Figure 1 shows an overview of the measurement setup. The dual-comb spectrometer follows the basic design discussed in refs. [20, 21]. It is based on two fully stabilized Er:fiber frequency combs with repetition rates of ≈200 MHz that are offset by 104 Hz. About 5–10 mW of mid-infrared light covering 4500–4900 nm is generated by nonlinear difference frequency generation between light at 1.07 and 1.35–1.4 μm originating from one frequency comb, as shown in Figure 1. The 1.07 μm light is generated by amplification of spectrally broadened light using a Yb-doped fiber amplifier. The 1.35–1.4 μm light is obtained by spectral broadening using highly nonlinear fiber. The

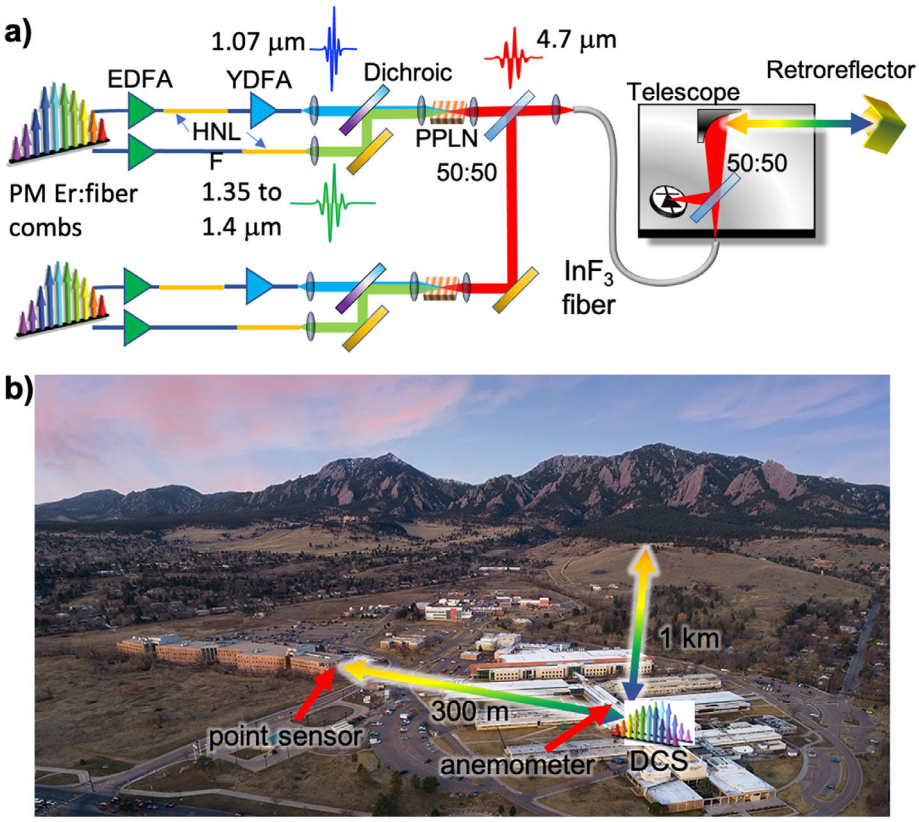

Figure 1. Overview. a) Schematic of open-path DCS system and telescope. PM: polarization maintaining. EDFA: erbium-doped fiber amplifier. HNLF: highly nonlinear fiber. YDFA: ytterbium-doped fiber amplifier. PPLN: periodically poled lithium niobate. b) The system is located in a room atop the NIST building in Boulder, CO, and the light is sent to a retroreflector located on a balcony of the NOAA building ≈300 m away. Alternatively, a second beam path launches the comb light to a reflector ≈1 km away. A point sensor at the NOAA building also records N_2O, CO, and H_2O concentrations. Wind speed and direction are recorded with a 3D sonic anemometer located on the roof of the NIST building.

mid-infrared light from both combs is combined on a free-space beam splitter and coupled into a single-mode InF_3 fiber, which runs to a telescope (Figure 1a). At the telescope, light is launched from the fiber tip, passes through a 50:50 beam splitter, and is collimated by an off-axis parabolic mirror (180 mm focal length, 10 cm diameter). About 1–1.5 mW of collimated light is sent through the atmosphere to a 12.5 cm diameter retroreflector located 300 m or 1 km away. After reflection, the light traverses the same path, reflects off the telescope's 50:50 beam splitter, with typically 10–30 µW collected after the beam splitter (see Figure S1 in the Supporting Information). Finally, the collected light is detected with a 250 MHz mercury cadmium telluride (MCT) detector.

The DCS system samples the atmosphere and generates a time-domain interferogram every 9.6 ms, as determined by the 104 Hz offset in the comb repetition rates. The interferograms are phase-corrected in real time and then coadded on a field-programmable gate array to give an averaged spectrum every ≈2 min,[20,24] as shown in **Figure 2**. The DCS spectra are fully resolved with a spectral point spacing of 200 MHz or 0.007 cm^{-1}. The resulting spectra are then analyzed to retrieve the path-averaged concentrations.[5,6] To do this, we must first divide the measured spectrum by the zero-absorption dual-comb spectrum, referred to as the baseline spectrum. Because the gas absorption spectra consist of narrow lines, we determine the slowly varying baseline by fitting the measured spectrum to a piecewise polynomial function that also includes the gas absorption profiles[5–7] (the CO_2 concentration is held fixed in this fit at its nominal value since its spectrum in this region includes a broad continuum component). The measured spectrum is then divided by this baseline to yield the open-path transmission spectrum. The transmission spectrum (Figure 2b) is fit by scaling each gas absorption model (Figure 2c) with a fit parameter proportional to the path-averaged concentration of each gas. The gas absorption models were calculated using spectral parameters from HITRAN2016.[41] For gases other than water, the fitted concentration is then corrected to the dry concentration without water present.

For comparison between DCS and a calibrated point sensor, an inlet was located at the retroreflector end of the 300 m path, as shown in Figure 1b. This inlet was connected to an off-axis cavity-enhanced spectrometer run by the National Oceanic and Atmospheric Administration (NOAA). This instrument measures N_2O, CO, and H_2O with a 1 Hz measurement rate (averaged to 1 min). Two standard gases were regularly delivered to the instrument inlet line throughout the five-day measurement period to evaluate instrument sensitivity between 317 and 385 ppb (nmol mol^{-1}) N_2O and 58 and 990 ppb CO. The standards were calibrated after the study using N_2O and CO standard tanks tied to the World Meteorological Organization (WMO) standards

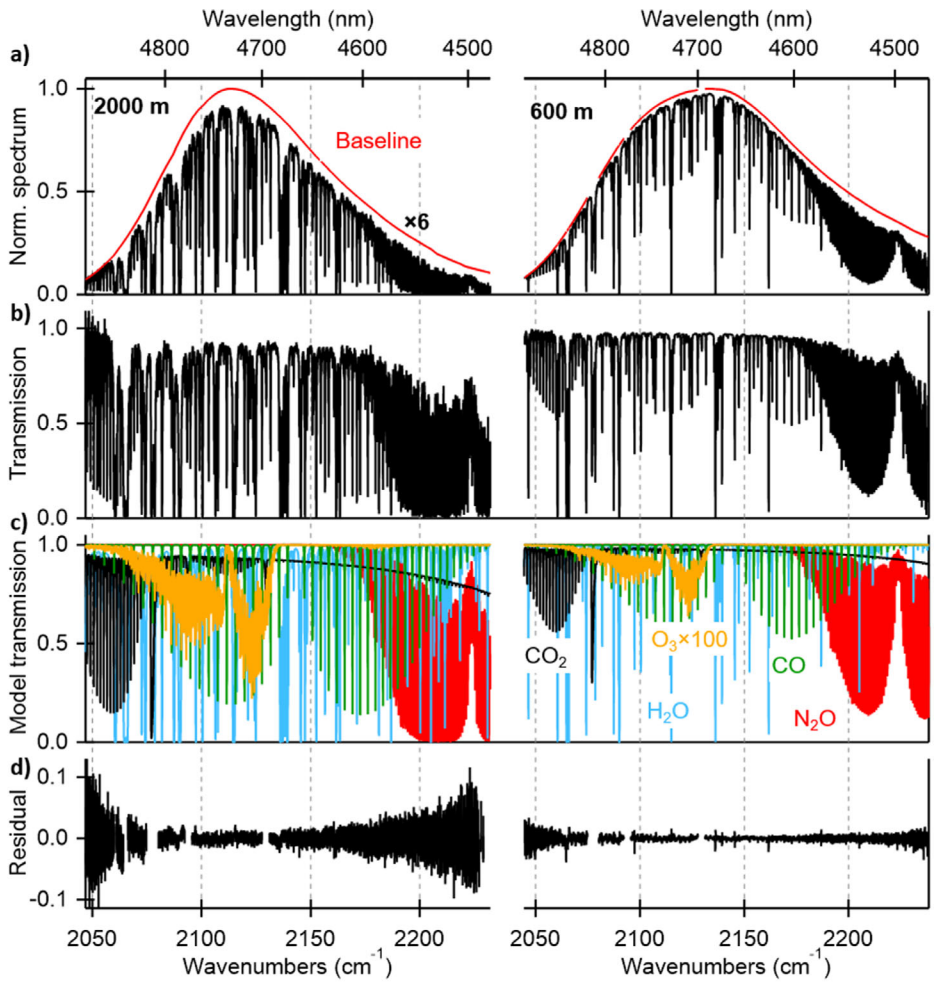

Figure 2. a) Measured return spectra for the 2000 and 600 m round-trip paths (black line). The overall shape reflects the comb spectra and is modeled as the baseline, or zero-absorption spectrum, shown as the red line. The strong atmospheric absorption appears as many deep narrow lines. b) Transmission, obtained by division of the measured spectrum with the baseline. c) Model transmission for CO_2, H_2O, CO, N_2O, and O_3 (100× magnified) for concentrations obtained by fitting the model to the transmission in (b). d) Residual obtained by subtracting the model (c) from the measured transmission (b).

WMO-N2O-X2006A and WMO-CO-X2014.[42] We estimate a total uncertainty of ±0.5 ppb for N_2O and ±0.8 ppb for CO. For O_3, there was no colocated point sensor. Instead, below we compare with data from a Colorado Department of Health and Environment (CDPHE) sensor located about 15 km north of the DCS open path that provided O_3 at 1 h temporal resolution. During this measurement campaign, there were no nearby operational CO_2 point sensors. Finally, the wind direction and speed were measured at 10 Hz with a 3D sonic anemometer located at the National Institute of Standards and Technology (NIST) building, as shown in Figure 1b.

3. Results

Figure 3 shows the measured path-averaged concentrations of N_2O, CO, CO_2, H_2O, and O_3 over five days of near-continuous measurements across the 600 m round-trip path at 2 min time resolution. In addition to the trace gas species, the DCS instrument retrieves the path-averaged temperature based on the fit. Also shown for comparison are the data from the point sensor located at NOAA for CO, N_2O, and H_2O (in blue) and from the CDPHE point sensor for O_3 (in red). In general, the DCS data compare well to the point sensor for slow, large-scale fluctuations indicative of well-mixed atmospheric conditions, while the point sensor's higher sensitivity for local concentration spikes is especially visible for CO. As discussed below, the DCS O_3 data are offset by +10 ppb in Figure 3. Because of the distance between the O_3 point sensor and the DCS instrument and the reactivity of O_3, we would not expect perfect agreement between the sensors; however, the slow trends are expected to roughly track as observed. For most of the gases, we observe significant fast and slow variability in concentrations due to the combination of atmospheric effects such as changing wind and planetary boundary layer height, and plumes from sources intersecting the beam path. During those time periods, O_3 varies between 0 and 50 ppb with noticeable diurnal variation arising from the fact that O_3 production is dominated by photochemical processes. The other criteria pollutant measured, CO, reaches a background level of ≈100

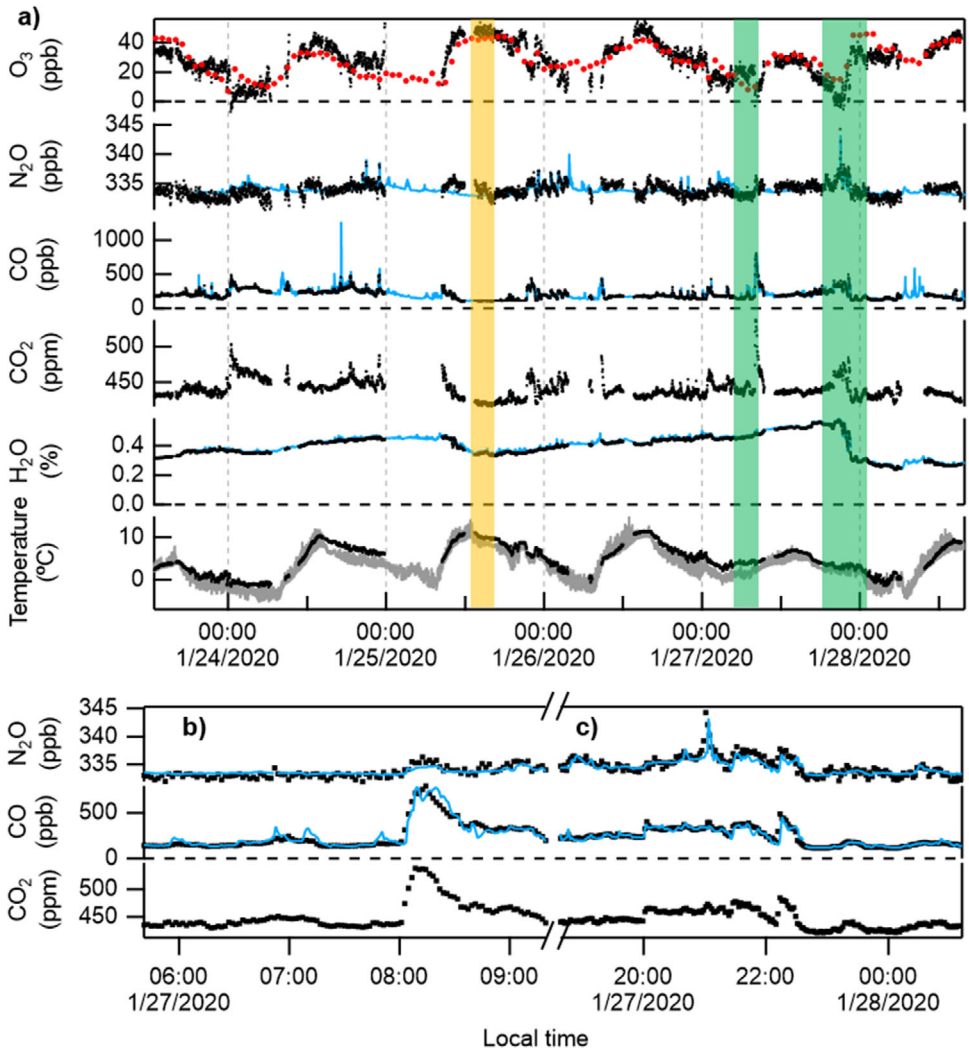

Figure 3. a) Retrieved path-averaged concentration and temperature for the DCS measurements (black) compared to measurements from in situ sensors (NOAA, blue; CDPHE, red dots; anemometer temperature, gray). Note that the retrieved O_3 concentration has been offset by 10 ppb. The orange-highlighted time period is used for the Allan deviation given in Figure 4b,c). An expanded view of the green highlighted regions in part (a), which are used for the N_2O versus CO_2 correlation plots in Figure 6.

ppb but shows large spikes up to ≈8× background due to local sources. Unlike the criteria pollutants, the GHGs CO_2 and N_2O show smaller variations relative to background, highlighting the need for high precision. This is especially true for N_2O where the background level is ≈330 ppb and the enhancements are only about 1–2% of the background. For CO_2, the background level reached ≈420 ppm (μmol mol^{-1}) with the largest spike ≈25% of the background.

We first use these data to evaluate the performance of the open-path DCS instrument for both sensitivity and bias. In order to determine the detection sensitivity for a trace gas, we evaluate the Allan–Werle deviation[43] over a time period with relatively constant concentrations when atmospheric variability is lower because the system is primarily measuring relatively clean air from the west (see orange highlighting in Figure 3). As seen in **Figure 4**, the Allan deviations average down linearly with the square root of averaging time for short averaging times until reaching a floor, with the exception of CO. For CO, we attribute the roughly constant 0.4 ppb sensitivity to true atmospheric variability, as it is consistent with the Allan deviation from the NOAA point sensor over the same time period. For CO_2, we also attribute the floor of the Allan deviation at 0.6 ppm to atmospheric variability, as it is consistent with similar data for CO_2 acquired with a near-infrared open-path DCS[6] at the same location. Note that the DCS spectrum was optimized for the detection of the other weaker gas species, so that the CO_2 absorption falls on the edge of the DCS spectrum. Nevertheless, because of the high CO_2 absorption cross-section in this spectral region, the sensitivity is comparable to near-infrared open-path DCS.[6] For O_3, we again attribute the 0.6 ppb floor to atmospheric variability as it is similar to the point-to-point variation measured by the CDPHE sensor at 1 h resolution. For N_2O, the Allan deviation reaches about 0.3 ppb and then appears to increase slightly at longer averaging times. By contrast, the point sensor at NOAA shows an Allan deviation

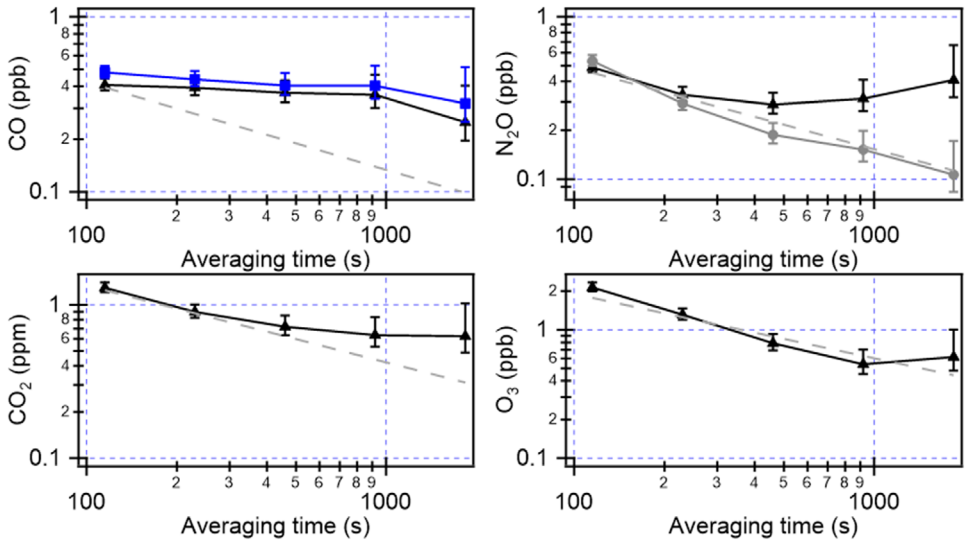

Figure 4. Allan–Werle deviation plots for the DCS measurements for CO, N_2O, CO_2, and O_3. Gray-dashed lines indicate the expected slope for white noise. The additional blue trace for CO is for the in situ point sensor. The additional gray trace for N_2O is the DCS data after correction for variation due to detector nonlinearity.

Table 1. Summary of fitted species and sensitivity for both measurement paths.

Gas	Spectral region [cm^{-1}]	Peak absorption (600 m)	Average concentration[a)]	Sensitivity@600 m and 2 min	Sensitivity@2 km and 2 min
N_2O	2150–2250	80%	334 ppb	0.5 ppb	0.88 ppb
CO	2075–2225	50%	202 ppb	0.4 ppb[b)]	0.6 ppb[b)]
CO_2	2040–2100	40%	440 ppm	1.3 ppm	1.9 ppm
O_3	2075–2130	0.4%	28 ppb	2 ppb	2.3 ppb
H_2O	2040–2250	100%	0.4%	11 ppm[b)]	56 ppm[b)]
Temp	Full	n/a	n/a	0.1 C	0.1 C

[a)] Concentration given in mole fraction: ppm = μmol mol^{-1}, ppb = nmol mol^{-1}; [b)] Sensitivity likely limited by atmospheric variability and not instrument noise.

that is flat at around 0.01 ppb. We attribute the ≈0.3 ppb limit to the DCS sensitivity for N_2O primarily to a small (<0.5%) time varying bias from nonlinearities discussed below. After correcting for this bias, the Allan deviation (gray) shows the expected linear trend.

Table 1 summarizes primary fitted gas species, their peak absorption, typical measured concentration, and the DCS sensitivity for both the 600 m and 2 km paths. Each molecule's spectral signature is shown in Figure 2. The spectral signal-to-noise ratio (SNR) on average was about 400 for a 115 s acquisition duration averaged over a spectral window of 2045–2240 cm^{-1}, which corresponds to an absorption sensitivity of 1/SNR = 0.0025 at the 200 MHz resolution. This SNR is defined as the point-to-point variations in the spectral response and is caused by detector noise, as shown in Figure S1 (Supporting Information). In order to estimate the detector-noise-limited concentration sensitivity for the DCS system, which simultaneously captures multiple absorption features of a single species, we need to do a numerical model as discussed in Figure S2 (Supporting Information). The results of this model show that this white noise contribution accounts for about half of the measured concentration variability, as given by the Allan deviation at 115 s. The additional noise terms are believed to be caused by time-dependent variations of the dual-comb spectrum, which are difficult to model numerically but also limit the sensitivity.

For the 2 km path, we did not observe over a long enough time period with low atmospheric variability to determine an Allan deviation, so the sensitivity is the standard deviation of a short, detrended time series. In the ideal case, the sensitivity would improve linearly with path length; however, the system is detector-noise-limited (as shown in Figure S1 in the Supporting Information) and the SNR is about 4 times lower for the 2 km path due to reduced return power, so the sensitivity for the 2 km path is slightly worse than that of the 600 m path. In addition to the main species listed in Table 1, we are also able to detect the isotopologues ^{13}CO, $^{13}CO_2$, $^{14}N^{15}NO$, $H_2{}^{18}O$, and $H_2{}^{17}O$ with δ-value precisions of 50‰, 5‰, 30‰, 20‰, and 60‰, respectively. Ratios of stable isotopes provide valuable information about the gas sources and sinks.[44] Open-path measurements of isotope ratios could be especially beneficial for water isotopologues because of the challenges associated with closed path sampling systems; however, currently the isotope ratio sensitivity of the open-path DCS is not high enough to be very useful for atmospheric measurements (typically on the order of 1‰ is desired).

Improvements to the return power and detector noise as well as longer averaging time should enable future isotope ratio measurements at the 1‰ level.

We also investigated potential sources of bias in the DCS measurements. To do this, we first compare the DCS measurements with the NOAA point sensor. As evident from the time series in Figure 3, the point sensor and DCS are well correlated. Their difference yields small, constant offsets (DCS − point sensor) of 1.8 ppb, −0.88 ppm, and −2.9 ppb for CO, H_2O, and N_2O, respectively, corresponding to percentage offsets of 0.9%, −0.02%, and −0.9%. These offsets are all within the known uncertainties of the HITRAN line parameters. We also evaluated the correlation between the DCS and NOAA sensors for CO, H_2O, and N_2O. The slope was 0.985 for CO, 0.991 for H_2O, and 1.0 for N_2O and with Pearson correlation coefficients of 0.91, 0.996, and 0.5, respectively. Again, these slopes are well within the uncertainties of the HITRAN database.

We can conduct a similar analysis for O_3 between the DCS measurements and the CDPHE point sensor. However, the different measurement timescales (2 minute vs 1 h) and the 15 km separation in locations make a direct comparison difficult. As noted earlier, we do find an ≈−10 ppb offset to the O_3 measurements from the DCS, which was corrected in Figure 3. This offset likely occurs because the O_3 absorption signal is very weak and fairly broad, which makes it susceptible to interference from inaccurate line shape models for the stronger species.[45] The ultrahigh resolution of the DCS system can greatly reduce the interference but only to the extent the spectral models are accurate. Improved line shape models or the inclusion of a persistent residual structure in the fit would help to reduce the O_3 offset.

For the N_2O retrievals, a small, time-varying bias does seem to be present in the data. This can be seen, for example, in the orange highlighted region in Figure 3 where the DCS measurements show more slow variability than the point sensor. These temporal variations are strongly correlated with the received optical power and are attributed to nonlinearities in the photodetector. By correcting for the temporal power variations, we were able to significantly reduce the N_2O variation during the time period used for the Allan deviation analysis (compare the gray and black data in Figure 4b). The N_2O power dependence is shown in Figure S3 (Supporting Information). This bias is low; we find a 0.6% change in N_2O with a factor of 2 change in received power. Nevertheless, this bias is significant for N_2O because of the low atmospheric variability and the high relative measurement sensitivity of 0.5/334 ppb = 0.15%. While this effect is possibly present for other gases as well, it is not significant compared to the atmospheric variability. In the future, this bias could be calibrated through laboratory measurements, and then a correction applied based on the measured received power, or the effect could be removed by using a lower nonlinearity MCT receiver.

4. Atmospheric Science Discussion

As discussed earlier, one of the significant advantages of multispecies detection is the ability to measure correlations between species. First, we focus on CO and CO_2. From Figure 3, it is already apparent that these two species are strongly correlated with both exhibiting a slowly varying background punctuated by larger spikes. This strong correlation is expected as they are both emitted from combustion sources, and the measurement site is located close to major roads. The variable background arises from atmospheric effects such as changing planetary boundary layer height, which effectively traps the emitted CO and CO_2 in a shallower or deeper box. The larger spikes are a result of gas plumes passing through the open-beam path. To analyze these plumes, we calculate the excess concentrations, CO_{xs} and CO_{2xs}, above a background level, determined using the robust baseline estimator approach.[46] As shown in **Figure 5**, CO_{xs} and CO_{2xs} are correlated with a slope of 5.28(4) ppb CO/ppm CO_2 (R^2 of 0.86). The tight correlation indicates that the combustion sources from these plumes have similar combustion efficiencies. Interestingly, we did observe a single plume event with a significantly higher CO_{xs}/CO_{2xs} ratio. Based on the wind and plume behavior, we believe that it is a local source, but the specific source is uncertain.

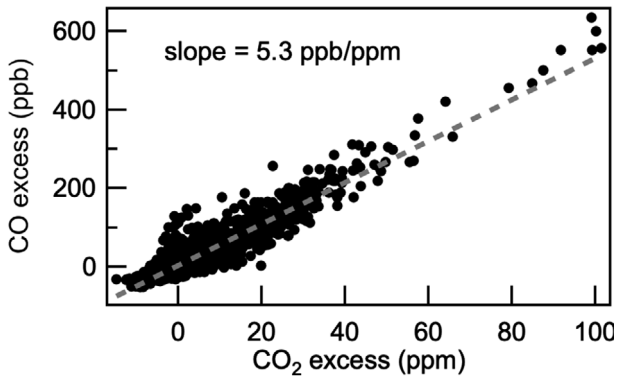

Figure 5. Correlation between excess CO and excess CO_2. The line fit is shown by the gray dashed line.

The expected ratio of CO versus CO_2 depends on the efficiency of combustion for a given source. Recent studies in urban areas have observed values between 4 and 8 ppb/ppm,[27,40,47,48] consistent with our value of 5.28 ppb/ppm. However, we do not find similar consistency between our measured ratio and one calculated from the US EPA National Emission Inventory (NEI 2017). If we just consider on-road mobile sources in Boulder County, the NEI yields a CO/CO_2 ratio of 17.9 ppb/ppm, which is significantly higher than the observed ratio (including additional sources beyond on-road mobile sources only further increasing the ratio). This discrepancy is consistent with previous studies,[27,40,47,48] which have suggested decreasing the NEI CO inventory by a factor of 2 to 3 to improve agreement with observations, although none of these previous studies were also in the same Denver area. Here, we find that the NEI overestimates CO by a slightly higher amount (about 3.4×), but without a longer duration data acquisition, it is difficult to estimate an uncertainty on this scaling. Furthermore, we do not have enough data to attribute whether any discrepancy is due to incorrect CO or CO_2 emissions in the NEI.

Next, we consider the N_2O sources. We expect that the observed N_2O enhancements arise primarily from vehicles where it is produced in catalytic converters, since any agricultural contribution is expected to be small in January. In the case of vehicle emissions, N_2O should be correlated with CO_2, just as with CO. However, traffic sources have a wide range of N_2O/CO_2 depending on the type of fuel source, type of catalytic converter,

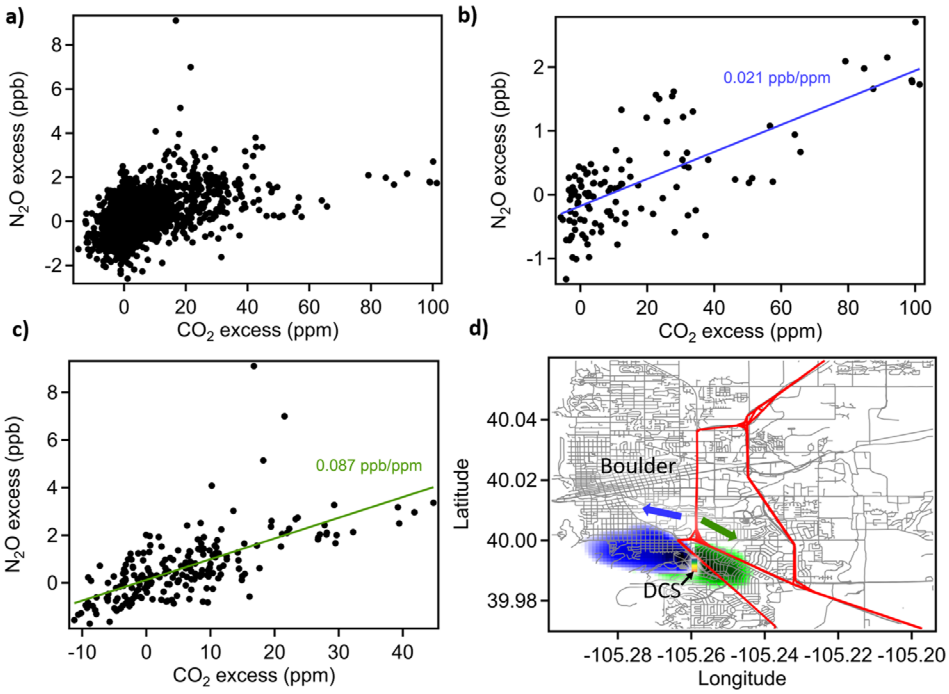

Figure 6. Correlation plots of excess N_2O versus excess CO_2 for a) all data and b,c) the green-shaded regions in Figure 3. Colored lines show the results from a line fit. d) Map of the estimated source footprints for the plume events in (b) (blue) and (c) (green) based on the wind direction and speed (indicated by blue and green arrows). Darker colors indicate a larger footprint. Major highways are indicated in red.

age of catalytic converter, and driving condition with values ranging from 0.004 ppb/ppm for low-emission, light-duty vehicles with new catalysts to 0.2 ppb/ppm for new diesel heavy-duty vehicles[49–52] (interestingly, N_2O/CO_2 ratios have been increasing for diesel vehicles as more advanced catalysts have been added to reduce NO_x emission[50,52]). From Figure 3, we do observe some correlation between N_2O and CO_2 but less correlation than between CO and CO_2. **Figure 6**a shows a scatter plot of excess N_2O versus excess CO_2, defined as previously for CO, over the full time period. Again, as expected, the correlation is far less tight than for the excess CO/CO_2 plot. This broad distribution suggests multiple source contributions with different N_2O/CO_2 ratios, perhaps due to temporal and spatial differences in traffic distributions combined with wind patterns. Based on Figure 6a, the range of correlation is ≈0.02–≈0.25 ppb/ppm, which is consistent with the range of values reported previously given above. Note that there are only a few points with the highest ratio, which arise from a very narrow plume event. The majority of points lie between 0.02 and 0.09 ppb/ppm. In order to better see the different source contributions, we plot the correlation for specific plume events, identified by the green shaded regions in Figure 3, in Figure 6b,c. These show much tighter correlation than for the entire time series. The slopes of the correlation plots for the two plume events are 0.021 and 0.087 ppb/ppm. To better understand the potential origin of these plume events and the difference in slope between them, we perform a footprint analysis as shown in Figure 6d. A footprint shows how much a source at a given grid cell will influence the concentration observed at a given receptor location and time and thus has units of concentration/area/time. We calculate the footprints using the Stochastic Time-Inverted Lagrangian Transport model's R Interface (STILT-R)[53] with a spatially uniform wind field generated from the local measurement. This analysis shows that the two events likely originate from different source locations and suggests that the first event (colored blue) arises from local traffic (which consists mostly of light-duty vehicles), whereas the second event (colored green) likely originates from highways with more truck traffic, leading to the higher slope.

5. Conclusions

We demonstrated open-path DCS measurements across a 600 m long path in the 4.5–5 µm spectral region for simultaneous measurements of CO, O_3, N_2O, CO_2, and H_2O. The system operated over five days with an 80% uptime. The 2 min sensitivities for N_2O, CO, CO_2, O_3, and H_2O were 0.5 ppb, 0.4 ppb, 1.5 ppm, 2 ppb, and 12 ppm, which are generally sufficient to capture atmospheric variations due to changes in the boundary layer or plumes from local sources. Furthermore, comparison with a colocated point sensor showed good agreement with small static offsets of 1.8 ppb, −0.88 ppm, and −2.9 ppb for CO, H_2O, and N_2O, respectively, which are attributed to uncertainties in the HITRAN data used for the retrievals.

In the future, several improvements are possible. First, the system can readily be extended to longer path lengths: we have tested the system over 2 km long paths and have demonstrated >5 km long paths in the near-infrared.[7] Second, with sensitivity improvements through higher power comb sources, lower relative-intensity noise and detector noise, and longer path lengths, the system could detect additional species and isotopologues at atmospherically relevant levels. These improvements would add even more information for source apportionment

and enable further applications. Similarly, with regard to air quality, future system improvements could enable high time resolution, sensitive O_3 measurements to develop a better understanding of the interplay between different factors influencing O_3 formation.[54,55]

The multispecies measurement capability of the instrument has clear applications to quantifying greenhouse gas emissions and validating emission inventories, as open-path dual-comb spectroscopy can now sense all four primary greenhouse gases, N_2O, CO_2, CH_4, and H_2O. In addition, the N_2O sensitivity is sufficient to enable temporally and spatially resolved N_2O flux characterization using a flux gradient approach[56] from agricultural sources and wetlands, which will help to constrain N_2O sources and enable monitoring of N_2O emission reduction measures.[37–39] From the data here, we provide initial correlation studies of both CO and N_2O with CO_2. Further extended deployments could provide a rich database for comparison with the NEI or other inventories and for guiding urban GHG reduction measures.

Supporting Information

Supporting Information is available from the Wiley Online Library or from the author.

Acknowledgements

The authors acknowledge valuable comments from B. R. Washburn and A. J. Fleisher. Funding was provided by NIST and the DARPA SCOUT program.

Conflict of Interest

The authors declare no conflict of interest.

Data Availability Statement

The data that support the findings of this study are available from the corresponding author upon reasonable request.

Keywords

dual-comb spectroscopy, greenhouse gas monitoring, mid-infrared spectroscopy, trace gas sensing

Received: December 22, 2020
Revised: April 30, 2021
Published online: June 30, 2021

[1] G. M. Russwurm, J. W. Childers, in *Handbook of Vibrational Spectroscopy* (Eds: J. M. Chalmers, P. R. Griffiths), John Wiley & Sons, Ltd, Hoboken, NJ, USA **2006**, pp. 1750–1773.
[2] T. E. L. Smith, M. J. Wooster, M. Tattaris, D. W. T. Griffith, *Atmos. Meas. Tech.* **2011**, *4*, 97.
[3] C.-H. Lin, R. H. Grant, A. J. Heber, C. T. Johnston, *Atmos. Meas. Tech.* **2020**, *13*, 2001.
[4] I. Coddington, N. Newbury, W. Swann, *Optica* **2016**, *3*, 414.
[5] G. B. Rieker, F. R. Giorgetta, W. C. Swann, J. Kofler, A. M. Zolot, L. C. Sinclair, E. Baumann, C. Cromer, G. Petron, C. Sweeney, P. P. Tans, I. Coddington, N. R. Newbury, *Optica* **2014**, *1*, 290.
[6] E. M. Waxman, K. C. Cossel, G.-W. Truong, F. R. Giorgetta, W. C. Swann, S. Coburn, R. J. Wright, G. B. Rieker, I. Coddington, N. R. Newbury, *Atmos. Meas. Tech.* **2017**, *10*, 3295.
[7] E. M. Waxman, K. C. Cossel, F. Giorgetta, G.-W. Truong, W. C. Swann, I. Coddington, N. R. Newbury, *Atmos. Chem. Phys.* **2019**, *19*, 4177.
[8] P. Ciais, P. Rayner, F. Chevallier, P. Bousquet, M. Logan, P. Peylin, M. Ramonet, *Clim. Change* **2010**, *103*, 69.
[9] S. Coburn, C. B. Alden, R. Wright, K. Cossel, E. Baumann, G.-W. Truong, F. Giorgetta, C. Sweeney, N. R. Newbury, K. Prasad, I. Coddington, G. B. Rieker, *Optica* **2018**, *5*, 320.
[10] C. B. Alden, S. C. Coburn, R. J. Wright, E. Baumann, K. Cossel, E. Perez, E. Hoenig, K. Prasad, I. Coddington, G. B. Rieker, *Environ. Sci. Technol.* **2019**, *53*, 2908.
[11] D. I. Herman, C. Weerasekara, L. C. Hutcherson, F. R. Giorgetta, K. C. Cossel, E. M. Waxman, G. M. Colacion, N. R. Newbury, S. M. Welch, B. D. DePaola, I. Coddington, E. A. Santos, B. R. Washburn, *Sci. Adv.* **2021**, *7*, eabe9765.
[12] K. C. Cossel, E. M. Waxman, F. R. Giorgetta, M. Cermak, I. R. Coddington, D. Hesselius, S. Ruben, W. C. Swann, G.-W. Truong, G. B. Rieker, N. R. Newbury, *Optica* **2017**, *4*, 724.
[13] Y. Jin, S. M. Cristescu, F. J. M. Harren, J. Mandon, *Opt. Lett.* **2014**, *39*, 3270.
[14] O. Kara, L. Maidment, T. Gardiner, P. G. Schunemann, D. T. Reid, *Opt. Express* **2017**, *25*, 32713.
[15] A. V. Muraviev, V. O. Smolski, Z. E. Loparo, K. L. Vodopyanov, *Nat. Photonics* **2018**, *12*, 209.
[16] O. Kara, F. Sweeney, M. Rutkauskas, C. Farrell, C. G. Leburn, D. T. Reid, *Opt. Express* **2019**, *27*, 21358.
[17] L. A. Sterczewski, J. Westberg, M. Bagheri, C. Frez, I. Vurgaftman, C. L. Canedy, W. W. Bewley, C. D. Merritt, C. S. Kim, M. Kim, J. R. Meyer, G. Wysocki, *Opt. Lett.* **2019**, *44*, 2113.
[18] G. Villares, A. Hugi, S. Blaser, J. Faist, *Nat. Commun.* **2014**, *5*, 5192.
[19] M. Yan, P.-L. Luo, K. Iwakuni, G. Millot, T. W. Hänsch, N. Picqué, *Light: Sci. Appl.* **2017**, *6*, e17076.
[20] G. Ycas, F. R. Giorgetta, E. Baumann, I. Coddington, D. Herman, S. A. Diddams, N. R. Newbury, *Nat. Photonics* **2018**, *12*, 202.
[21] G. Ycas, F. R. Giorgetta, K. C. Cossel, E. M. Waxman, E. Baumann, N. R. Newbury, I. Coddington, *Optica* **2019**, *6*, 165.
[22] A. S. Kowligy, H. Timmers, A. J. Lind, U. Elu, F. C. Cruz, P. G. Schunemann, J. Biegert, S. A. Diddams, *Sci. Adv.* **2019**, *5*, eaaw8794.
[23] Z. Chen, T. W. Hänsch, N. Picqué, *Proc. Natl. Acad. Sci. USA* **2019**, *116*, 3454.
[24] G. Ycas, F. R. Giorgetta, J. T. Friedlein, D. Herman, K. C. Cossel, E. Baumann, N. R. Newbury, I. Coddington, E. Baumann, E. Baumann, N. R. Newbury, I. Coddington, *Opt. Express* **2020**, *28*, 14740.
[25] T. Holloway, H. Levy, P. Kasibhatla, *J. Geophys. Res.: Atmos.* **2000**, *105*, 12123.
[26] S. Newman, S. Jeong, M. L. Fischer, X. Xu, C. L. Haman, B. Lefer, S. Alvarez, B. Rappenglueck, E. A. Kort, A. E. Andrews, J. Peischl, K. R. Gurney, C. E. Miller, Y. L. Yung, *Atmos. Chem. Phys.* **2013**, *13*, 4359.
[27] J. C. Turnbull, C. Sweeney, A. Karion, T. Newberger, S. J. Lehman, P. P. Tans, K. J. Davis, T. Lauvaux, N. L. Miles, S. J. Richardson, M. O. Cambaliza, P. B. Shepson, K. Gurney, R. Patarasuk, I. Razlivanov, *J. Geophys. Res.: Atmos.* **2015**, *120*, 292.
[28] H. S. Halliday, J. P. DiGangi, Y. Choi, G. S. Diskin, S. E. Pusede, M. Rana, J. B. Nowak, C. Knote, X. Ren, H. He, R. R. Dickerson, Z. Li, *J. Geophys. Res.: Atmos.* **2019**, *124*, 10951.
[29] D. E. Ward, L. F. Radke, in *Dahlem Workshop Reports: Environmental Sciences Research Report 13* (Eds: P. J. Crutzen, J. G. Goldammer), John Wiley & Sons, Chichester, England **1993**, pp. 53–76.

[30] R. J. Yokelson, D. W. T. Griffith, D. E. Ward, *J. Geophys. Res.: Atmos.* **1996**, *101*, 21067.
[31] D. A. Jaffe, N. L. Wigder, *Atmos. Environ.* **2012**, *51*, 1.
[32] M. Jerrett, R. T. Burnett, C. A. Pope, K. Ito, G. Thurston, D. Krewski, Y. Shi, E. Calle, M. Thun, *N. Engl. J. Med.* **2009**, *360*, 1085.
[33] X. Li, Y. Choi, B. Czader, A. Roy, H. Kim, B. Lefer, S. Pan, *Atmos. Chem. Phys.* **2016**, *16*, 3127.
[34] J. E. Diem, *Environ. Pollut.* **2003**, *125*, 369.
[35] M. Masiol, S. Squizzato, D. Chalupa, D. Q. Rich, P. K. Hopke, *Sci. Total Environ.* **2019**, *654*, 1167.
[36] L. Cheadle, L. Deanes, K. Sadighi, J. G. Casey, A. Collier-Oxandale, M. Hannigan, *Sensors* **2017**, *17*, 2072.
[37] H. Tian, R. Xu, J. G. Canadell, R. L. Thompson, W. Winiwarter, P. Suntharalingam, E. A. Davidson, P. Ciais, R. B. Jackson, G. Janssens-Maenhout, M. J. Prather, P. Regnier, N. Pan, S. Pan, G. P. Peters, H. Shi, F. N. Tubiello, S. Zaehle, F. Zhou, A. Arneth, G. Battaglia, S. Berthet, L. Bopp, A. F. Bouwman, E. T. Buitenhuis, J. Chang, M. P. Chipperfield, S. R. S. Dangal, E. Dlugokencky, J. W. Elkins, B. D. Eyre, B. Fu, B. Hall, A. Ito, F. Joos, P. B. Krummel, A. Landolfi, G. G. Laruelle, R. Lauerwald, W. Li, S. Lienert, T. Maavara, M. MacLeod, D. B. Millet, S. Olin, P. K. Patra, R. G. Prinn, P. A. Raymond, D. J. Ruiz, G. R. van der Werf, N. Vuichard, J. Wang, R. F. Weiss, K. C. Wells, C. Wilson, J. Yang, Y. Yao, *Nature* **2020**, *586*, 248.
[38] X. Zhang, E. A. Davidson, D. L. Mauzerall, T. D. Searchinger, P. Dumas, Y. Shen, *Nature* **2015**, *528*, 51.
[39] D. S. Reay, E. A. Davidson, K. A. Smith, P. Smith, J. M. Melillo, F. Dentener, P. J. Crutzen, *Nat. Clim. Change* **2012**, *2*, 410.
[40] O. E. Salmon, P. B. Shepson, X. Ren, H. He, D. L. Hall, R. R. Dickerson, B. H. Stirm, S. S. Brown, D. L. Fibiger, E. E. McDuffie, T. L. Campos, K. R. Gurney, J. A. Thornton, *J. Geophys. Res.: Atmos.* **2018**, *123*, 7705.
[41] I. E. Gordon, L. S. Rothman, C. Hill, R. V. Kochanov, Y. Tan, P. F. Bernath, M. Birk, V. Boudon, A. Campargue, K. V. Chance, B. J. Drouin, J.-M. Flaud, R. R. Gamache, J. T. Hodges, D. Jacquemart, V. I. Perevalov, A. Perrin, K. P. Shine, M.-A. H. Smith, J. Tennyson, G. C. Toon, H. Tran, V. G. Tyuterev, A. Barbe, A. G. Császár, V. M. Devi, T. Furtenbacher, J. J. Harrison, J.-M. Hartmann, A. Jolly, T. J. Johnson, T. Karman, I. Kleiner, A. A. Kyuberis, J. Loos, O. M. Lyulin, S. T. Massie, S. N. Mikhailenko, N. Moazzen-Ahmadi, H. S. P. Müller, O. V. Naumenko, A. V. Nikitin, O. L. Polyansky, M. Rey, M. Rotger, S. W. Sharpe, K. Sung, E. Starikova, S. A. Tashkun, J. V. Auwera, G. Wagner, J. Wilzewski, P. Wcisło, S. Yu, E. J. Zak, *J. Quant. Spectrosc. Radiat. Transfer* **2017**, *203*, 3.
[42] B. D. Hall, G. S. Dutton, J. W. Elkins, *J. Geophys. Res.: Atmos.* **2007**, *112*, D09305.
[43] P. Werle, R. Mücke, F. Slemr, *Appl. Phys. B* **1993**, *57*, 131.
[44] T. J. Griffis, *Agric. For. Meteorol.* **2013**, *174–175*, 85.
[45] C. Frankenberg, P. Bergamaschi, A. Butz, S. Houweling, J. F. Meirink, J. Notholt, A. K. Petersen, H. Schrijver, T. Warneke, I. Aben, *Geophys. Res. Lett.* **2008**, *35*, L15811.
[46] A. F. Ruckstuhl, M. P. Jacobson, R. W. Field, J. A. Dodd, *J. Quant. Spectrosc. Radiat. Transfer* **2001**, *68*, 179.
[47] G. Plant, E. A. Kort, C. Floerchinger, A. Gvakharia, I. Vimont, C. Sweeney, *Geophys. Res. Lett.* **2019**, *46*, 8500.
[48] I. Lopez-Coto, X. Ren, O. E. Salmon, A. Karion, P. B. Shepson, R. R. Dickerson, A. Stein, K. Prasad, J. R. Whetstone, *Environ. Sci. Technol.* **2020**, *54*, 2606.
[49] M. E. Popa, M. K. Vollmer, A. Jordan, W. A. Brand, S. L. Pathirana, M. Rothe, T. Röckmann, *Atmos. Chem. Phys.* **2014**, *14*, 2105.
[50] D. C. Quiros, J. Smith, A. Thiruvengadam, T. Huai, S. Hu, *Atmos. Environ.* **2017**, *168*, 36.
[51] L. A. Graham, S. L. Belisle, P. Rieger, *Atmos. Environ.* **2009**, *43*, 2031.
[52] T. J. Wallington, P. Wiesen, *Atmos. Environ.* **2014**, *94*, 258.
[53] B. Fasoli, J. C. Lin, D. R. Bowling, L. Mitchell, D. Mendoza, *Geosci. Model Dev.* **2018**, *11*, 2813.
[54] A. J. Abeleira, D. K. Farmer, *Atmos. Chem. Phys.* **2017**, *17*, 6517.
[55] T. Bien, D. Helmig, *Elementa: Sci. Anthropocene* **2018**, *6*, 55.
[56] T. K. Flesch, V. S. Baron, J. D. Wilson, D. W. T. Griffith, J. A. Basarab, P. J. Carlson, *Agric. For. Meteorol.* **2016**, *221*, 111.

